Spin-Orbit Torques in Laminated Tungsten Multilayers with Nominally Doped Oxygen

James Lourembam[1]*, Hong Jing Chung[1], Lisen Huang[1], Khoong Hong Khoo[2], Jinjun Qiu[1], Huiqing Xie[1], DV Maheswar Repaka[1], Sherry Lee Koon Yap[1], Hang Khume Tan[1], Bingjin Chen[2], Seng Kai Wong[1], Abhijit Ghosh[1], Haidong Liang[3], Sabpreet Bhatti[4], T.S. Suraj[5], Andrew Anthony Bettiol[3], Anjan Soumyanarayanan[5,1], SN Piramanayagam[4], Sze Ter Lim[1]*

[1]*Institute of Materials Research and Engineering (IMRE), Agency for Science, Technology and Research (A*STAR), 2 Fusionopolis Way, Innovis, Singapore 138364, Singapore*

[2]*Institute of High Performance Computing (IHPC), Agency for Science, Technology and Research (A*STAR), 1 Fusionopolis Way, #16-16, Connexis North, Singapore 138632*

[3]*Centre for Ion Beam Applications (CIBA), Department of Physics, National University of Singapore, Singapore 117542*

[4]*Division of Physics and Applied Physics, School of Physical and Mathematical Sciences, Nanyang Technological University, 637371, Singapore*

[5]*Physics Department, National University of Singapore, 117551 Singapore*

*Correspondence should be sent to james_lourembam@imre.a-star.edu.sg, lim_sze_ter@imre.a-star.edu.sg

Abstract

Spin–orbit torque (SOT) control of magnetization is being rapidly positioned for energy-efficient computing across various memory hierarchies. Concurrently, the study of intrinsic and extrinsic factors, such as doping, to enhance SOT is of considerable scientific interest. Here, we introduce 2% nominally doped oxygen via post-deposition oxygen flow in β-phase tungsten, one of the most promising SOT materials, to create laminated [W/O] structures. Incorporating them in annealed multilayer stacks compatible with industrial production, we find ~50% enhancement in spin Hall angle with minimal compromise in intrinsic spin Hall conductivity. Furthermore, we integrate [W/O] into SOT magnetic tunnel junctions achieving ~30% reduction in critical switching current densities while maintaining a relatively large tunnel magnetoresistance (>135%). Our findings highlight that engineering nominal doping in established SOT materials offers an attractive alternative for accelerating materials development for SOT magnetic random-access memory (MRAM).

I. Introduction

Manipulation of magnetic moments using spin–orbit torques (SOT) is one of the leading approaches for next-generation cache memory solutions and energy-efficient computing. Spintronic memories are inherently non-volatile making them advantageous over existing technologies in normally-off computing architectures [1]. SOT-based spintronic memories possess additional attractive device features such as sub-nanosecond switching, extremely high endurance due to decoupled read and write paths, CMOS compatibility and low write-error rates [2–4]. The working principle of an SOT device is the conversion of charge current to pure spin current in a non-magnetic spin-orbit coupling layer [5]. This conversion ratio described as the spin Hall angle is the most critical material optimization parameter for SOT-based technologies. Several exotic materials including topological insulators, and Weyl semimetals have been investigated to enhance effective spin Hall angle, θ_{SH}^{eff} [6–9]. However, materials compatibility with industrial processes on large-scale 200 mm or 300 mm wafers and integration with established magnetic tunnel junction stacks remain limited to normal metals, primarily Ta, W, and Pt. Among these β-W has been shown to have the highest θ_{SH}^{eff} with most reports citing ~ −0.3 and reaching up to −0.6 in some as-deposited W films [10–14]. In addition, β-W incorporated stacks can be integrated into magnetic tunnel junctions (MTJ) of either in-plane or perpendicular magnetic anisotropy, which show large tunnel magnetoresistance (TMR). However, on industrial sputtering tools with annealing requirements for MTJ fabrication, β-W can only be grown up to a thickness of ~4 nm [4]. At such ultra-low thicknesses, the crystalline quality of β-W is poor [15] and θ_{SH}^{eff} does not reach its upper range [14]. Furthermore, an ultra-thin SOT layer presents endpoint etching challenges over the entire wafer.

Recently, to further enhance θ_{SH}^{eff} in β-W while concomitantly widening the thickness window, dopants such as Ta, O, N etc. have been introduced [14,16–19]. When an O dopant is introduced during sputtering, the θ_{SH}^{eff} of β-W is reported to be −0.5 [17]. O doping leads to bond lengthening allowing stabilization of the larger β-W crystal [19]. While extrinsic mechanisms can significantly influence θ_{SH}^{eff} in the presence of impurities, simulations [18] and experiments [17] on O-doped W indicated they have limited impact. Experimental θ_{SH}^{eff} did not significantly change with increasing O doping. In fact, intrinsic spin-Hall conductivity σ_{SH} was found to decrease with increasing O dopants and is related to θ_{SH}^{eff} as $\theta_{SH}^{eff} = \sigma_{SH}\rho_{xx}\Gamma$, where ρ_{xx} is the longitudinal resistivity and Γ is the interfacial spin transparency [14]. These works were carried out with large O doping (10 – 44%) where high ρ_{xx} plays a larger role in determining θ_{SH}^{eff}. However, high resistivity is undesirable in computing devices as it increases power consumption and increases vulnerability to electrical failure [20].

Sethu *et al.* introduced an alternative method of O doping by using multilayer laminated structures [W/O] where an oxygen flow of 300 s is introduced after the deposition of each W layer [16]. This approach is more industry-friendly as post-deposition oxygen flow can be incorporated in a dedicated chamber without breaking vacuum, eliminating the possibility of oxygen contamination in other layers. β phase was found to stabilize up to ~9 nm and θ_{SH}^{eff} was reported to be −0.32 at 6 nm thickness. However, θ_{SH}^{eff} was determined using harmonic Hall method which is prone to large planar Hall angle contribution in W, necessitating a deeper investigation of θ_{SH}^{eff} [14]. Moreover, the percentage of O doping using this deposition approach was not reported though it is expected to be much lower. Additionally, the TMR in

MTJ stacks incorporating [W/O] was found to be surprisingly lower than that of intrinsic β-W (<100 %).

Here, we adopt O-doped laminated W structures, [W/O] for SOT channel using a significantly reduced oxygen flow (15 s) with the aim of minimal doping while extending the β phase thickness window. We also investigate θ_{SH}^{eff} using both spin-torque ferromagnetic resonance and harmonic Hall methods and find it to be ~−0.35 in annealed β-[W/O] at 6 nm thickness. Comparing between annealed films, [W/O] has higher θ_{SH}^{eff} than even pristine β-W. Using first principles calculations, we demonstrate the benefits of minimal O doping in mitigating the degradation of σ_{SH}, which drops to values even lower than α-W at >11% doping. The β-[W/O] heterostructures are then adopted to fabricate SOT-MTJs on 200 mm wafers. They perform significantly better than those with β-W on the metric of switching current density while retaining similarly high TMR values (>100%).

II. Samples and Methods

The films are deposited on 200 mm Si/SiO_2 wafers in a Singulus Timaris magnetic sputtering system. The pristine W films are deposited with 100 W power and 120 sscm Ar gas flow. The [W/O] multilayers are deposited by introducing oxygen plasma with 30 W power and Ar:O sscm gas flow ratio at 220:15 for 15s in a separate chamber without breaking vacuum. The films are annealed at 300 °C for 1 hour in vacuum and cooled naturally.

X-ray photoelectron spectroscopy (XPS) measurements are performed on a PHI Quantera SXM Scanning X-ray Microprobe with a monochromatic Al $K\alpha$ source. X-ray Diffraction (XRD) studies are carried using D8 DISCOVER (Bruker) with IμS microfocus Cu X-ray source. Micromag Alternating Gradient Magnetometry (AGM) is used to determine saturation magnetization at room temperature (RT). Cross-section Transmission Electron Microscopy of the films are conducted using Tecnai G2 F20. Rutherford backscattering spectrometry of the [W/O] thin films is carried out at the Centre for Ion Beam Applications at the National University of Singapore.

To further understand the results, we perform first-principles Density Functional Theory (DFT) calculations as implemented in the VASP code [21]. We also study the spin Hall conductivity (SHC) by employing the Kubo formula [22] with matrix elements and energy eigenvalues obtained on a dense k-point grid through Wannier interpolation [23].

III. Results and Discussion

A. Structure of [W/O] multilayers

Two sets of films are prepared — (i) pristine W films and (ii) $[W(t)/O]_{n-1}$/ W(t) multilayer films. The thickness of each layer in nanometres is represented by t, while n represents number of repeats. The second set of films, which terminates with a W layer, is labelled [W/O] hereafter unless otherwise stated. The total thickness of the SOT channel layer is represented as t_{CH} (in parenthesis), where $t_{CH} = t\times n$. This approach allows us to vary t_{CH} while maintaining consistent oxygen exposure by keeping t constant and varying n. The deposition of [W/O] multilayer films includes a short 15 s oxidation step (methods). Since MTJ stacks require annealing for the crystallization of CoFeB/MgO layers [24], all films are annealed

unless otherwise stated. For the pristine W films consistent with previous reports the β phase does not survive > 5 nm (Figure 1a) upon 300 °C annealing as shown by the X-ray diffraction 2θ scans (Figure 1a). However, we find that our [W/O] multilayer films retain the β phase up to 9 nm even after 300 °C annealing (Figure 1b) similar to Sethu *et al.* [16]. Notably, the grain size (6-8 nm) is larger in our [W/O] multilayer films (Appendix A, Figure 6) compared to the nanocrystalline W(O) films (< 4 nm) prepared by directly introducing oxygen during sputtering which have a large O concentration of 10 – 40% [17]. The critical thickness for the β to α phase transition can also be independently verified by resistivity measurements. For the resistivity measurements study on [W/O], a wedge multilayer $[W(t)/O]_3/W(t)$ is deposited. The resistivity values of the α phase are much lower (< 50 μΩ·cm) compared to the β phase (>100 μΩ·cm). Figure 1c shows that after annealing, the critical phase transition thickness has doubled in [W/O] multilayer films compared to W films.

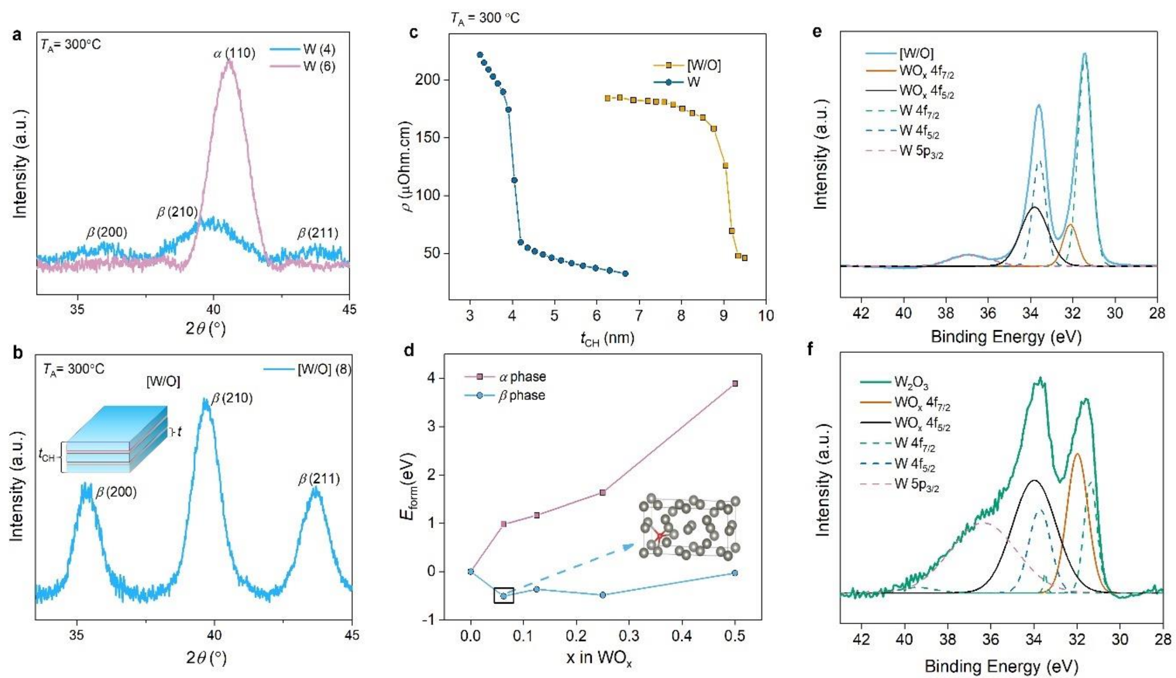

Figure 1. Structure of [W/O] multilayers. (a) XRD spectra of pristine W films showing β (4 nm) and α phase (6 nm). (b) XRD spectra of a $[W(2)/O]_3/W(2)$ multilayer film stabilized in the β phase. (c) Comparison of resistivity vs film thickness plot for films annealed at 300 °C. A wedge multilayer $[W(t)/O]_3/W(t)$ is chosen to represent the [W/O] samples for the resistivity measurements, where $t_{CH} = 4t$. (d) Formation energies as a function of increasing oxygen content determined from first-principles calculations. Inset is a schematic of the $WO_{0.0625}$ crystal structure where the grey (red) spheres represent W (O) atoms. XPS spectra of (e) $[W(2)/O]_3/W(2)$ multilayer and (f) W_2O_3 (10) films at W 4*f* core level. The dashed lines indicate the constituent peaks used in the fitting.

To understand the stabilization of β-W upon oxygen exposure, we look at the formation energy with oxygen dopants using first-principles calculations. As shown in Figure 1d, the calculated formation energy per O atom (E_{form}) monotonically increases with dopant

concentration for α-W, likely due to increased strain and dopant repulsion in the system with increasing O concentration, and thus reducing its stability. However, for β-W, E_{form} as a function of dopant concentration remains relatively flat at low doping and increases slightly at high doping. This demonstrates the strong binding that exists between W and O atoms which offsets the tendency to increase E_{form}. Additionally, the difference in E_{form} between O-doped β-W and α-W increases with dopant concentration. This implies a consistent conclusion that O-doping of W tends to stabilize β-W with respect to α-W. The low-doping regime is more relevant for our [W/O] multilayer films, whereas Demasius *et al.* W(O) films [17] fall in the high doping regime.

The oxidation states in [W/O] multilayer films have not been reported so far and we seek to address this using XPS and RBS techniques. The XPS spectra near the W 4*f* region, is shown in Figure 1e. The peaks at binding energies of 31.4 eV and 33.6 eV belong to W $4f_{7/2}$ and W $4f_{5/2}$, respectively. The constituent peaks at 32.1 eV and 33.8 eV which arise from the asymmetry in the W 4*f* doublet peaks indicates oxidation of W [19]. These features are similar to those of W(O) films albeit at a significantly lower O concentration [19]. As a comparison, we also perform XPS measurements on W_2O_3 sputtered from a target of the same composition. Here, the peaks are broader and the relative intensities of the constituent peaks at 32.1 eV and 33.8 eV are stronger showing a marked contrast with [W/O] multilayers.

The composition of the [W/O] multilayer films is examined using RBS technology, which is accurate and widely used to determine the composition of thin films [25–27]. The experimental and fitted spectra of a representative film (Appendix A, Figure 7) reveal that the atomic concentration of oxygen is approximately 2% for our 15 s oxidation step.

B. Spin-Hall angle of [W/O] multilayers

Next, we investigate θ_{SH}^{eff} of our [W/O] multilayer films using the harmonic Hall method [14,28,29]. Here, we fabricate two sets of Hall bar devices with the stack configurations $[W(2)/O]_2$/W(2)/CoFeB(1)/MgO and $[W(1.5)/O]_5$/W(1.5)/CoFeB(1)/MgO. All Hall bar devices are annealed at 300 °C. The Hall measurements are carried out at room temperature on a sample holder with both polar (θ) and azimuthal (φ) rotation w.r.t. applied field, B. The Hall measurement configuration of applied field, applied current, and magnetization vectors is shown in inset of Figure 2a. The first (R^{ω}) and second Hall resistances ($R^{2\omega}$) taken in the anti-damping-like configuration for $[W(2)/O]_2$/W(2)/CoFeB(1)/MgO Hall bar are shown in Figure 2a which are then used to calculate the anti-damping-like (B_{AD}) term (Appendix B). Similar measurements are also performed for the field-like configuration to determine the field-like (B_{FL}) term. The final value of θ_{SH}^{eff} is determined from the coupled expression of B_{AD} and B_{FL} terms (Appendix B) and is found to be large ($|\theta_{SH}^{eff}| > 0.3$), comparable with many reported values of β-W. The comparison with θ_{SH}^{eff} from W(t)/CoFeB(1)/MgO is also shown in Figure 2b. Here, the sharp drop in θ_{SH}^{eff} for t >5 nm corresponds to the α-W transition. Crucially, we note that the highest modulus value of θ_{SH}^{eff} (−0.23) achieved in the pristine W film is smaller than that of $[W(2)/O]_2$/W(2) multilayer film (−0.35). Meanwhile, a moderate ~12% reduction in $|\theta_{SH}^{eff}|$ is

found for the $[W(1.5)/O]_5/W(1.5)$ multilayer film. However, our calculations for θ_{SH}^{eff} are carried out assuming planar Hall contribution to be zero. Typically, W-based heterostructures have large planar Hall effect (PHE) which could lead to inaccurate values of θ_{SH}^{eff} from the harmonic Hall method [14].

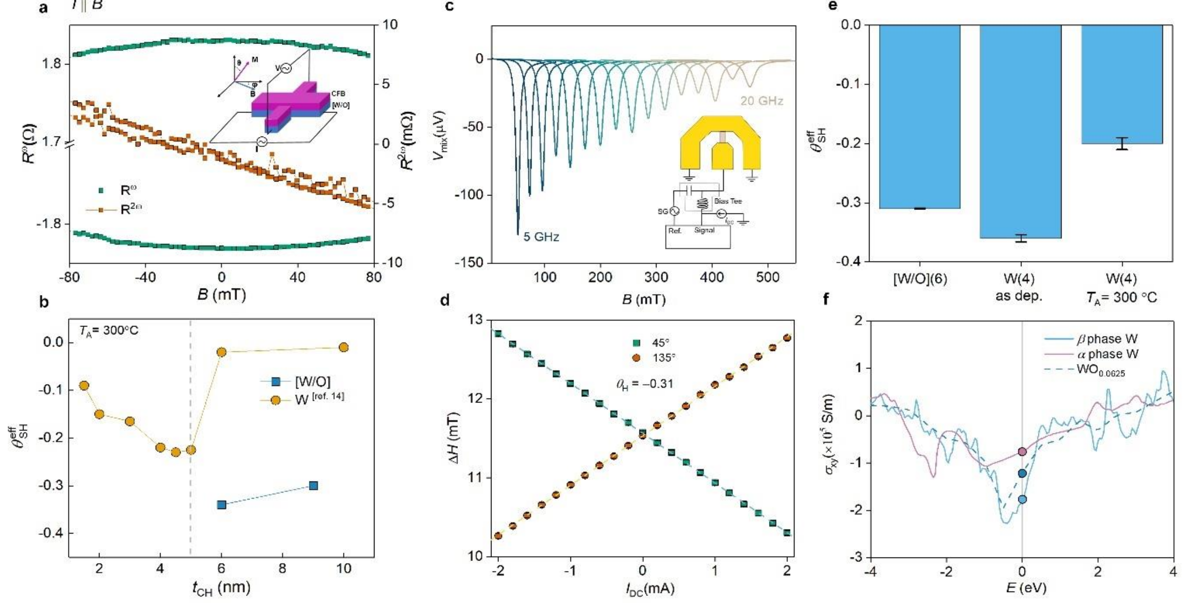

Figure 2. Spin-Hall effect from W/O multilayers. (a) First and second harmonic Hall resistances measured in the anti-damping-like configuration. Inset represents schematic of the measurement geometry along with the stack configuration. (b) Anti-damping spin Hall angle of [W/O] multilayers compared with pristine W at various film thicknesses. All films are annealed at 300 °C. The [W/O] data points at 6 nm and 9 nm in the SOT channel correspond to the multilayers $[W(2)/O]_2/W(2)$ and $[W(1.5)/O]_5/W(1.5)$, respectively. (c) ST-FMR spectra of [W/O](6)/CoFeB(1.5)/MgO stack taken at frequencies between 5 and 20 GHz. Inset shows the measurement configuration. (d) ST-FMR linewidth as a function of DC current on the same device. The dashed lines represent linear fittings. (e) Comparison of anti-damping spin Hall angle as determined by ST-FMR for various W-based films. (f) Spin Hall conductivities near the Fermi level of α and β phases of pristine W along with that of β-$WO_{0.0625}$ determined from first-principles calculations.

Therefore, we adopt spin-torque ferromagnetic resonance (ST-FMR) technique as an additional verification step to quantify θ_{SH}^{eff}. Moreover, ST-FMR is more suitable for determining θ_{SH}^{eff} of in-plane anisotropy samples such as as-deposited films [30]. Figure 2c shows the FMR spectra of the 300˚C-annealed $[W(2)/O]_2/W(2)$/CoFeB(1.5)/MgO measured by ST-FMR. Strong resonance signals are detected in the microwave range of 5 GHz to 20 GHz. When applying an additional direct current (I_{DC}) during the ST-FMR measurement, the linewidth ΔH of the spectrum can be modified by the current direction and strength. Figure 2d shows the dependence of ΔH on I_{DC} showing a clear linear relationship. We calculate θ_{SH}^{eff} to be −0.31 for the [W/O] multilayers from the average value of the slopes measured at θ

=45° and 135°, where θ is the angle between I_{DC} and applied field, B (Figure 2d). Similarly, θ_{SH}^{eff} of the reference sample W(4)/CoFeB(1.5)/MgO is extracted. Figure 2(e) summarizes θ_{SH}^{eff} of the β-[W/O] and β-W SOT heterostructures. The as-deposited β-W(4) reference sample has the largest spin Hall angle, consistent with previous reports [13], but is reduced to −0.21 after annealing. Meanwhile the [W/O] SOT heterostructure maintains a relatively large value at −0.31 even after annealing. This indicates that the [W/O] multilayer films are better at retaining β-phase after annealing. Although a higher θ_{SH}^{eff} was reported in W(O) samples where O is introduced during the deposition, the measurements were carried out in as-deposited samples and had a much higher O concentration. [17] Those samples, consequently, had higher resistivity reaching up to ~400 μΩ·cm. The spin Hall angle obtained from the ST-FMR measurements is very close to the values calculated from the Harmonic Hall measurements in Figure 2(b). This suggests that that the dominant contribution to θ_{SH}^{eff} comes from anti-damping torque, and the assumption of PHE ~0 is reasonable for this system. For high levels of O doping (>10%) in W, it has been argued that θ_{SH}^{eff} is primarily interfacial in origin [17]. To investigate the role of O doping at the heavy metal-ferromagnet interface we fabricated a control sample with oxygen termination: $[W(2)/O]_3$/CoFeB (1.5)/MgO annealed at 300°C for ST-FMR measurements. We found the magnitude of θ_{SH}^{eff} increased to −0.36 (Appendix B, Figure 10).

Next, we examine intrinsic spin Hall conductivity (σ_{SH}) calculated from first-principles calculations as a function of the Fermi level (E_F) position for α-W, β-W, and β-WO_x structures (Figure 2f). Since our samples are minimally O doped, we choose the $WO_{0.0625}$ (6% doping) structure for comparison. If we focus on the σ_{SH} at E_F = 0 eV, we see that β-W has the largest σ_{SH} with a value of −1797 S/cm, and this is a result of multiple band crossings close to the Fermi level that contribute strongly to σ_{SH}. However, these features are less prevalent in α-W, giving rise to a smaller σ_{SH} of −760 S/cm. The introduction of O-dopants in β-W perturbs the band structure and reduces the number of band crossings near E_F, thus reducing σ_{SH} to −1202 S/cm but still higher than that of α-W. Higher O doping (x >0.125, 11% doping) lowers the absolute value of σ_{SH} to even further than that of α-W (Appendix C, Figure 12). This change in σ_{SH} with doping concentration may account for the moderate reduction in experimental θ_{SH}^{eff} for $[W(1.5)/O]_5/W(1.5)$ compared to $[W(2)/O]_2/W(2)$ as determined from harmonic Hall. First-principles calculations represent the upper limit of intrinsic spin-charge conversion and as previously mentioned longitudinal resistivity and interfacial spin transparency factors affect experimental θ_{SH}^{eff}. Moreover, ultra-thin β-W films suffer from lower crystalline quality which may worsen upon annealing. A combination of these factors can be attributed to the smaller experimental value of θ_{SH}^{eff} in β-W compared to [W/O] multilayers. Extrinsic spin Hall calculations using the semiclassical Boltzmann formalism show that their contribution is negligible when oxygen doping in tungsten is ≤11% [18]. Therefore, for the $[W(2)/O]_2/W(2)$ multilayer, which has 2% doping, we expect negligible but non-zero extrinsic contributions to θ_{SH}^{eff}. It is possible that extrinsic effects could be enhanced by increasing oxygen doping, for example, by reducing the layer thickness (t).

C. SOT-MTJ with [W/O] current channel

To demonstrate the superiority of [W/O] multilayers as the SOT channel we integrate them into MTJ stacks. We fabricate in-plane (IP)-MTJs where the long-axis of the ellipse is perpendicular to the direction of SOT current flow as shown in Figure 3a. In this configuration, the MTJ can be electrically switched field-free [31] and simplifies direct comparison with pristine W channel. The film stack for IP-MTJ stack consists of the bottom $Co_{40}Fe_{40}B_{20}$ (t_{CoFeB}) which acts as the free layer (FL), while the 2.6 nm $Co_{40}Fe_{40}B_{20}$ fixed layer is antiferromagnetically coupled to the 2.6 nm CoFe which is pinned by the PtMn layer. Several MTJs of sizes 200 nm × 400 nm with different CoFeB (CFB) free layer thickness (t_{CFB}) are fabricated. The IP-MTJ devices are annealed at 330°C for 2 hours with an in-plane magnetic field of 1 Tesla applied parallel to long-axis of the ellipse in high-vacuum environment. All MTJs are etched till the heavy metal SOT channel.

The [W/O] SOT channel thickness is fixed at 6 nm which has higher θ_{SH}^{eff} than 9 nm (Figure 2b). Indeed, we find that these MTJs can be switched without any external field over a wide range of electrical pulses (10 ns – 1 μs). A representative example of the switching for t_{CFB} =1.33 nm is shown in Figure 3b. The switching voltage threshold increases upon reducing the pulse width as expected [31]. We then compare the switching current densities (J_c) of MTJs with β-[W(2)/O]$_2$/W(2) (filled symbols) vs. those with β-W(4) (open symbols) SOT channels as shown in Figure 3c. For the same CFB thickness, we see that MTJs with the [W/O] channel consistently show lower switching current densities. The critical current density, J_{c0} in this MTJ configuration can be described by an established spin-transfer torque model described by [32,33]

$$J_c = J_{c0}[1 - \frac{\ln(t_p)}{\Delta}]$$

where Δ is the thermal stability of the MTJ and t_P is the applied pulse width, assuming 1 ns of thermal attempt time. By fitting the above equation to Figure 3(b), we find J_{c0} to be 1.3 ×10^7 A/cm^2 for t_{CFB} =1.33 nm providing a 27% reduction using β-[W/O] over β-W. Similarly, a 34% reduction in J_0 is observed for t_{CFB} =1.5 nm. These improved switching results (~30% reduction) are consistent with the higher θ_{SH}^{eff} obtained from ST-FMR and Hall measurements. Assuming one-spin model, J_{c0} is given by the expression [3,34]

$$J_{c0} = \frac{2e}{\hbar}\frac{\mu_0 M_s t_{CFB}\alpha}{\theta_{SH}^{eff}}(H_c + \frac{M_{eff}}{2})$$

where e is the elementary charge, $\hbar$ is the reduced Planck's constant, μ_0 is the permeability of free space, and H_C is the coercive field. Using film-level materials parameters for damping, α = 0.017, saturation magnetization, M_S = 1.4 ×10^6 A/m, effective magnetization, $4\pi M_{eff}$ = 0.4 T, we calculate θ_{SH}^{eff} ~ −0.11, which is significantly lower than that determined from ST-FMR and harmonic Hall effect. It should be noted that similar discrepancy has been reported in previous W-based MTJs [16]. The discrepancy can be attributed to multi-domain switching, and role of temperature [16].

Furthermore, to demonstrate that β-[W/O] is the primary SOT channel for in-plane SOT MTJs, we also need to show its superiority over Pt, which is widely adopted in in-plane MTJs [31]. It is to be noted that Pt does not have stringent channel thickness requirement like β-W. The most significant advantage of β-[W/O] over Pt lies in its ability to provide much higher TMR and enable tunability of the free layer thickness without compromising on the TMR. Figure 3d shows that the TMR with the β-[W/O] multilayer SOT channel remains high (135% –180%). The TMR with a Pt channel is strongly dependent on CFB thickness and is projected to be dramatically reduced to 14% at t_{CFB} =1.3 nm [31].

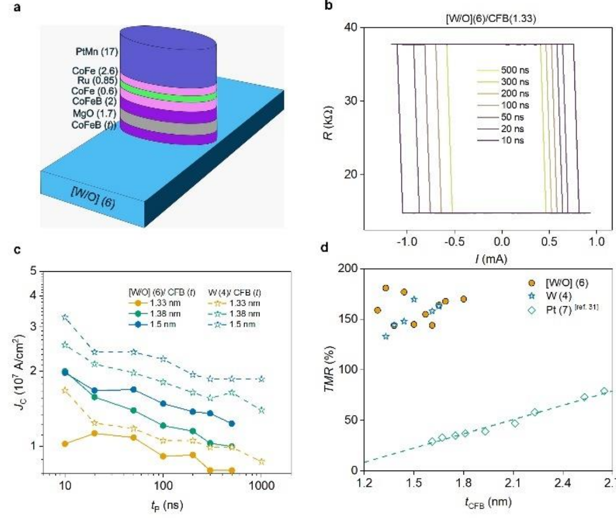

Figure 3. W/O multilayers-based SOT-MRAM cell. (a) Schematic of the IP SOT-MTJ with the [W/O] multilayers as the writing channel. (b) Pulse width-dependent SOT switching of the same MTJ at t_{CFB} = 1.33 nm. (c) Comparison of switching current densities between the β-[W/O] (filled symbols) and β-W (open symbols). Switching current densities at 3 different CoFeB thicknesses are also shown. (d) Comparison of CoFeB thickness-dependent TMR of SOT-MTJs fabricated with β-[W/O] and β-W channels.

It was previously reported that utilizing a combination of O and N gases in the W channel, W(O,N), would reduce the critical SOT current densities in field-assisted perpendicular (p)-MTJs by about 25% but the TMR concurrently was reduced to 80% [16]. It was argued that the W(O,N) may be more susceptible to process damage. In our case, we do not observe any such compromise in TMR even in p-MTJs using [W/O] multilayers as the SOT channel (Appendix, Figure 13). These p-MTJs can be switched by SOT but require a small in-plane offset field of ~5 mT. Finally, the MTJs with β-$[W(2)/O]_2/W(2)$ as the SOT channel have a much higher yield performance across the 200 mm wafer than those with β-W(4).

IV. Conclusion

In conclusion, we demonstrated that our β-[W/O] multilayer films are superior to β-W in two crucial device metrics: spin-Hall angle and switching current density for the development of

practical SOT-MRAM on a wafer-level platform. Nominally doped oxygen via lamination provides an attractive route to achieving high spin-Hall angle for thicker, annealed films even with a slight reduction in theoretical spin-Hall conductivity. Successful adoption of β-[W/O] channel is demonstrated in IP-MTJs. Incorporating this SOT channel for field-free perpendicular MTJ architectures would be of immediate value in commercializing energy-efficient, and scalable memory beyond STT-MRAM.

Acknowledgements

This work was supported by the SpOT-LITE programme (A*STAR grant no. A18A6b0057), funded by Singapore's RIE2020 initiatives.

Appendix A: Material characterization of [W/O] multilayers

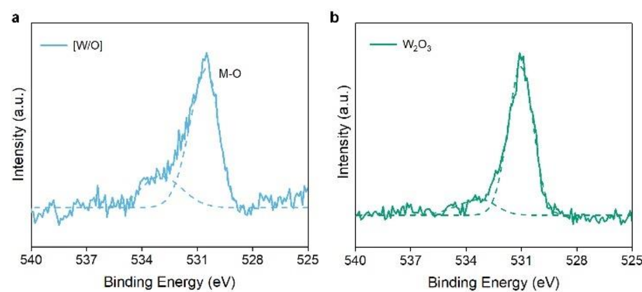

Figure 4. Core level O 1*s* XPS spectra for (a) $[W(2)/O]_3/W(2)$ multilayer and (b) W_2O_3 (10) films showing the W-O bond. The dashed lines indicate the two constituent peaks used in the fitting. The primary peaks centered at ~530 eV can be ascribed to the O-W bonds while the other peak at ~533 eV is assigned to surface O-H bonds.

.

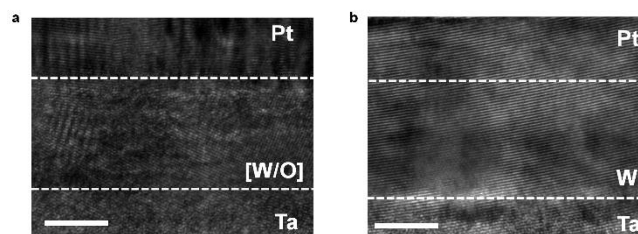

Figure 5. Cross-section transmission electron microscopy images of (a) Ta(5)/[W/O](9) /Pt(5) multilayer and (b) Ta(5)/W(9)/Pt(5) films. The white scale bar is 5 nm. The [W/O] multilayer film shows density layering while the pristine W film shows uniform crystallinity.

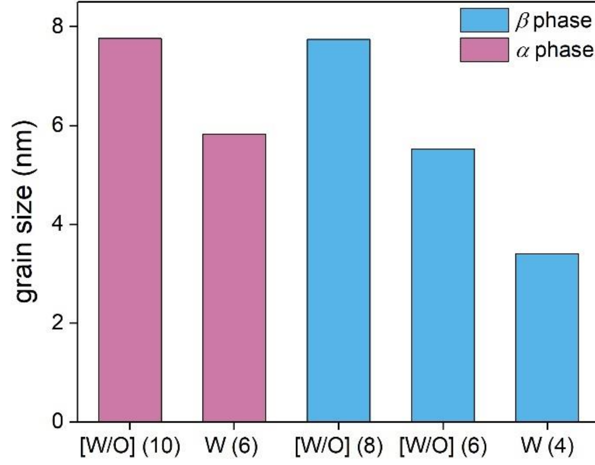

Figure 6. Comparison of grain sizes of various W-based films obtained from the XRD data using the Scherrer equation. We calculate the grain size (d_g) of the annealed films using the Scherrer equation $d_g = \frac{\lambda}{\beta cos\theta}$ where wavelength, λ = 0.154 nm, β is the full-width at half maximum and θ is the diffraction angle of the XRD measurements. We observe that the grain size increases upon increasing the film thickness i.e. thicker β-W films have larger crystallite size.

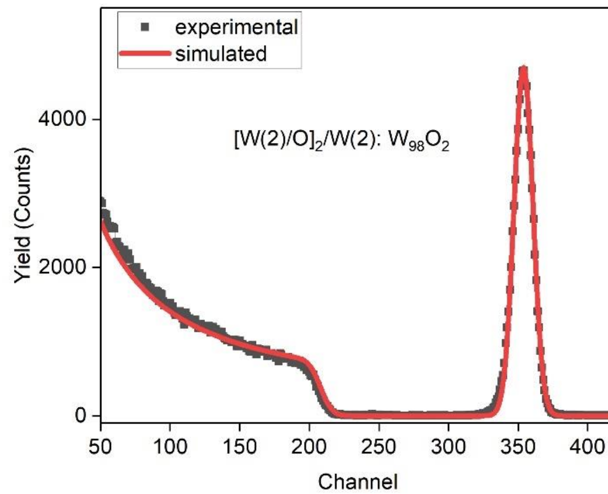

Figure 7. Rutherford backscattering of $[W(2)/O]_2/W(2)$ structures and fitting curves of corresponding to $W_{98}O_2$ stoichiometry. The energy of Helium ions is 500 keV, and the detector is positioned at 90 degrees.

Appendix B. Spin-Hall characterization of [W/O] multilayers

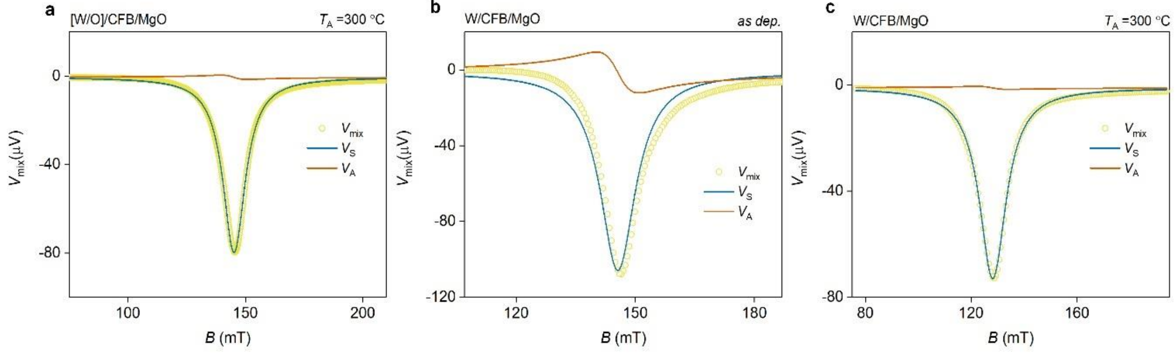

Figure 8. Rectifying voltage of the sample $[W(2)/O]_2/W(2)/CoFeB$ (1.5)/MgO annealed at 300˚C (a), as-deposited W(4)/CoFeB(1.5)/MgO (b) and W(4)/CoFeB(1.5)/MgO annealed at 300˚C (c), measured by the ST-FMR technique at the microwave frequency of 9 GHz and power of 5 dBm.

For the ST-FMR measurements a signal generator is used to source microwave with a frequency range of 5 – 20 GHz. The microwave amplitude is modulated by a low frequency of 317.3 Hz. The rectifying voltage V_{mix} is measured by the lock-in amplifier at the same frequency. An external in-plane field (B_x) is swept at 45° / 135° with reference to the direction of microwave. The measured V_{mix} consists of a symmetric Lorentz spectrum (blue curve) induced by the damping-like torque and an antisymmetric spectrum (dark red curve) resulting from the field-like torque and the Oersted field. Both the symmetric and the antisymmetric Lotrentz spectra share the common resonance field H_r and the linewidth ΔH. The relationship can be expressed as $V_{\mathrm{mix}} = V_{\mathrm{S}} \frac{(\Delta H/2)^2}{(B-H_{\mathrm{r}})^2+(\Delta H/2)^2} + V_A \frac{(B-H_{\mathrm{r}})(\Delta H/2)}{(B-H_{\mathrm{r}})^2+(\Delta H/2)^2}$, where B is the applied magnetic field, V_s and V_A are the amplitude of the symmetric and antisymmetric Lorentz curve, respectively. We were able to obtain both H_r and ΔH by fitting the curve with the equation. For all the three samples, the signal is dominated by the symmetric component, i.e. the damping-like torque.

Using the Kittel fitting on the resonance field vs. frequency plot, we extract the effective magnetization $4\pi M_{eff}$ and the gyromagnetic ratio γ. The linear dependence of the linewidth on the frequency gives the damping constant of 0.017.

Here, the Oersted field is negligibly small due to the small current flowing into the device strip.

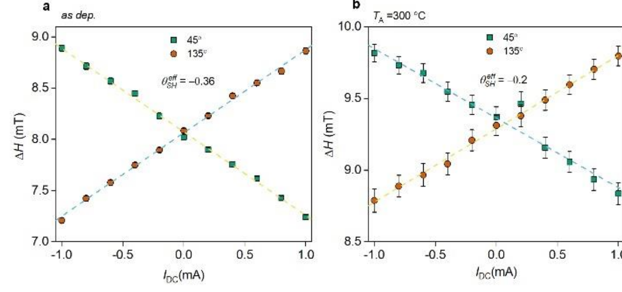

Figure 9. Modulation of line-width (ΔH) by applied d.c. current (I_{DC}) for (a) as-deposited and (b) 300˚C annealed W(4)/CoFeB(1.5)/MgO films during ST-FMR measurement. When a direct current is applied to the device, it modifies the damping constant and hence the linewidth. The magnetic field is applied at the angle of 45˚ and 135˚ to the microwave/current direction. The ST-FMR is measured at the microwave frequency of 6 GHz and power of 5 dBm. A linear relationship is established between the linewidth and the current, which can be expressed as $\frac{\partial \Delta H}{\partial J_c} = \frac{4\pi f}{\gamma} \frac{sin\theta}{(H_r + 2\pi M_{eff})\mu_0 M_s t} \frac{\hbar}{2e} \theta_{SH}^{eff}$. [30] Here J_c is the current density, f is the microwave frequency, θ is the angle between the applied magnetic field, B and I_{DC}, γ is the gyromagnetic ratio, $4\pi M_{eff}$ is the effective magnetization, M_s is the saturation magnetization (1000 emu/cc), and t is the thickness of the CoFeB. M_{eff} and γ can be extracted from the Kittel fitting of the resonance field vs. frequency plot.

Here we took the average value of the slopes measured at 45˚ and 135˚ to calculate θ_{SH}^{eff}. The as-deposited 4 nm-W has a θ_{SH}^{eff} of −0.36, similar to reported values for β-phase W. [13,30] After annealing at 300˚C, θ_{SH}^{eff} reduces to −0.2. Correspondingly, the device resistance also reduces from 918 Ω to 846 Ω. Annealing may partially transform β-phase to α-phase, which has a much smaller spin Hall angle.

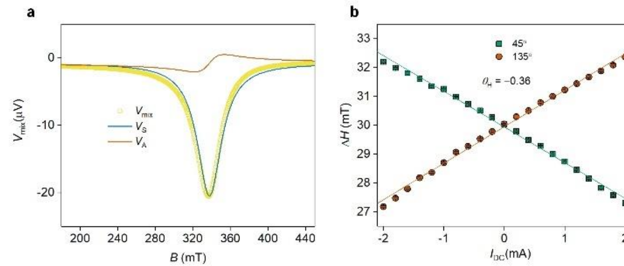

Figure 10. ST-FMR measurements on the oxygen-terminated film [W(2)/O]$_3$/CoFeB (1.5)/MgO annealed at 300˚C. a) Rectifying voltage (V_{mix}) of the sample measured at the microwave frequency of 9 GHz. V_S and V_A represent the amplitudes of the symmetric and antisymmetric components of the fitted Lorentz curve. b) Modulation of line-width (ΔH), measured at the microwave frequency of 9 GHz, by applied d.c. current (I_{DC}) for films during ST-FMR measurement. $\theta_{SH}^{eff} = -0.36$ is determined from the average value of the linear slopes measured at two ST-FMR configurations, where the magnetic field is applied at angles of 45˚ and 135˚ to the microwave/current direction. The spin Hall angle of the oxygen-terminated sample is found to be slightly higher than that of the tungsten-terminated sample.

Harmonic Hall analysis. The harmonic hall measurements are carried in three φ (angle between current, I and applied magnetic field, B_{ext}) values. The anti-damping-like (B_{AD}) and the field-like (B_{FL}) terms of the SOT coupled expression are carried out in $\varphi = 0°$ and $\varphi = 90°$, respectively. We also measure at the configuration $\varphi = 45°$ to quantify the planar Hall resistance (R_{P}) which has mixed contributions from both B_{AD} and B_{FL}. The SOT coupled expression is given by [14,28,29]

$$\begin{pmatrix} B_{AD} \\ B_{FL} \end{pmatrix} = \frac{1}{1-4\eta^2} \begin{pmatrix} 1 & 2\eta \\ 2\eta & 1 \end{pmatrix} \begin{pmatrix} \Gamma_{\parallel} \\ \Gamma_{\perp} \end{pmatrix}$$

where $\Gamma_{\parallel}$ and $\Gamma_{\perp}$ are related to first (R^{ω}) and second Hall resistances ($R^{2\omega}$) as $\Gamma_{\parallel} = \frac{dR^{2\omega}/dB}{d^2R^{\omega}/dB^2}|_{\varphi=0°}$ and $\Gamma_{\perp} = \frac{dR^{2\omega}/dB}{d^2R^{\omega}/dB^2}|_{\varphi=90°}$. η is the ratio of anomalous Hall resistance to planar Hall resistance. For our W/CFB/MgO and [W/O]/CFB/MgO heterostructures, we find $\eta \sim 0.7$ which leads to non-physical values of B_{AD} and B_{FL}. Instead θ_{SH} calculations are done assuming $\eta = 0$ following previous reports for similarly high η. [14]

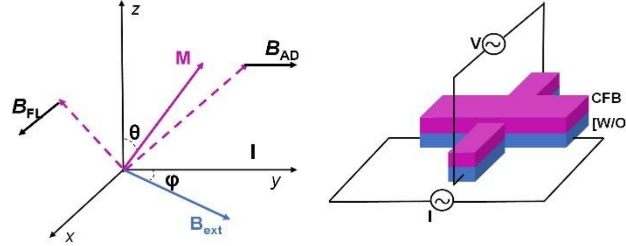

Figure 11. Schematic of the SOT harmonic hall measurements along with the anti-damping-like (B_{AD}) and the field-like (B_{FL}) components in cartesian co-ordinate system. The relative orientations of magnetization (M) applied magnetic field (B_{ext}) and applied current (I) are also shown. The dashed pink lines indicate M components in the yz and zx planes.

Appendix C. Spin Hall conductivity from first-principles calculations

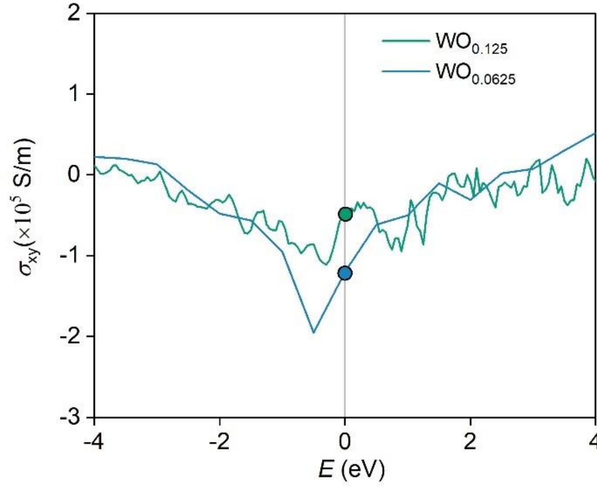

Figure 12. Comparison of spin Hall conductivities (σ_{SH}) near fermi level for $WO_{0.0625}$ and $WO_{0.125}$ determined from first-principles calculations. Higher doping leads to lower absolute values of σ_{SH}. The O doping percentage in $WO_{0.125}$ is 11.1%. The additional calculation at higher oxygen doping shows that $|\sigma_{SH}|$ reduces with increasing O concentrations.

Ionic potentials are treated using the Projector Augmented Wave (PAW) method [35] and exchange-correlation is approximated using the Perdew-Burke-Ernzerhof parametrization of the Generalized Gradient Approximation (GGA-PBE). [36] Electron wavefunctions are represented using plane waves with an energy cutoff of 400.0 eV and the Brillouin zone is sampled using the Monkhorst-Pack [37] grid with a spacing of 0.15 $Å^{-1}$. Also, the atomic positions are relaxed until the force component per atom is less than 0.02 eV/Å.

To compute the formation energy E_{form} for O-doping in W, we first generate 16 atom supercells of α-W (2×2×2) and β-W (2×1×1) and incorporate O atoms in high symmetry positions at various dopant concentrations. We then fully relax these systems and take the energy difference between these O-doped systems and bulk W / isolated O_2 as reference to evaluate E_{form}. We also study the spin Hall conductivity (SHC) of pristine and doped W, and this is achieved by employing the Kubo formula [22] with matrix elements and energy eigenvalues obtained on a dense k-point grid through Wannier interpolation. [23] In particular, k-point grids of 100×100×100 and 60×60×60 are used for unit cells of α-W and β-W systems respectively to converge the SHC as a function of Fermi level position. For SHC calculations of $WO_{0.0625}$, we use a (2×1×1) supercell of β-W with a single O-dopant and a k-point grid of 30×60×60.

Appendix D. Perpendicular SOT-MTJ with [W/O] multilayer channel

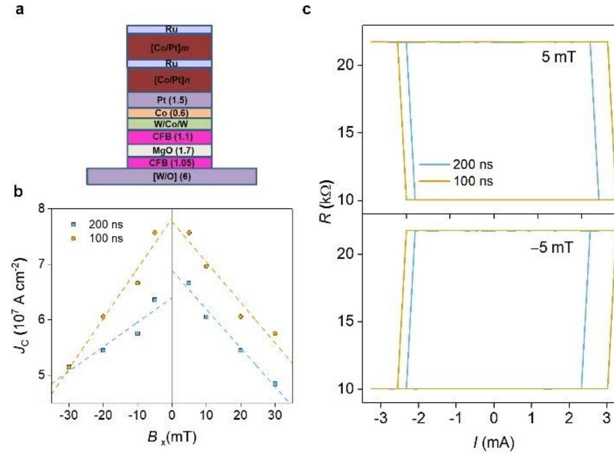

Figure 13. Schematic of the SOT perpendicular (p)-MTJ stack with the [W/O] multilayers as the writing channel. The bottom $Co_{20}Fe_{60}B_{20}$ (1.05) which acts as the free layer (FL), while the 1.1 nm $Co_{20}Fe_{60}B_{20}$ is the fixed layer which is coupled to the [Co/Pt]-based synthetic antiferromagnet. The fabrication process of the p-MTJ is similar to the IP-MTJs with two main differences. The films are annealed at 300 °C without field and the MTJs are patterned into circular shapes of diameter 240 nm. (b) Dependence of SOT switching current density (J_C) as a function of small in-plane field (B_x). Here, both the applied field and the pulse voltage and are along the x-direction. In this configuration, it is expected to have linear relationship between J and B_x. [38] Upon extrapolating the linear fitting, the field-free current density, $J_C^{B=0}$ (i.e. B_x =0) at 100 ns and 200 ns are estimated to be 7.7 $\times 10^7$ A/cm^2 and 6.6 $\times 10^7$ A/cm^2, respectively (c) SOT switching of the p-MTJ shown at 5 mT bias field (top panel) and −5 mT bias field (bottom panel).

References

[1] H.Yoda, S.Fujita, N.Shimomura, E.Kitagawa, K.Abe, K.Nomura, H.Noguchi, and J.Ito, *Progress of STT-MRAM Technology and the Effect on Normally-off Computing Systems*, in *Proc. Int. Electron Devices Meet.* (2012), p. 259–262.

[2] B. Dieny, I. L. Prejbeanu, K. Garello, P. Gambardella, P. Freitas, R. Lehndorff, W. Raberg, U. Ebels, S. O. Demokritov, J. Akerman et al., Opportunities and challenges for spintronics in the microelectronics industry, Nat Electron **3**, 446 (2020).

[3] S. Shi, Y. Ou, S. V. Aradhya, D. C. Ralph, and R. A. Buhrman, Fast low-current spin-orbit-torque switching of magnetic tunnel junctions through atomic modifications of the free-layer interfaces, Phys Rev Appl **9**, 11002 (2018).

[4] K. Garello, F. Yasin, S. Couet, L. Souriau, J. Swerts, S. Rao, S. Van Beek, W. Kim, E. Liu, S. Kundu et al., *SOT-MRAM 300mm Integration for Low Power and Ultrafast Embedded Memories*, in *IEEE Symp. VLSI Circuits, Honolulu, HI* (2018), p. 81–82.

[5] A. Manchon, J. Železný, I. M. Miron, T. Jungwirth, J. Sinova, A. Thiaville, K. Garello, and P. Gambardella, Current-induced spin-orbit torques in ferromagnetic and antiferromagnetic systems, Rev Mod Phys **91**, 035004 (2019).

[6] N. H. D. Khang, Y. Ueda, and P. N. Hai, A conductive topological insulator with large spin Hall effect for ultralow power spin–orbit torque switching, Nat Mater **17**, 808 (2018).

[7] I. Shin, W. J. Cho, E. S. An, S. Park, H. W. Jeong, S. Jang, W. J. Baek, S. Y. Park, D. H. Yang, J. H. Seo et al., Spin–Orbit Torque Switching in an All-Van der Waals Heterostructure, Advanced Materials **34**, 2101730 (2022).

[8] J. Han, A. Richardella, S. A. Siddiqui, J. Finley, N. Samarth, and L. Liu, Room-Temperature Spin-Orbit Torque Switching Induced by a Topological Insulator, Phys Rev Lett **119**, 077702 (2017).

[9] D. MacNeill, G. M. Stiehl, M. H. D. Guimaraes, R. A. Buhrman, J. Park, and D. C. Ralph, Control of spin-orbit torques through crystal symmetry in WTe 2 /ferromagnet bilayers, Nat Phys **13**, 300 (2017).

[10] J. Liu, T. Ohkubo, S. Mitani, K. Hono, and M. Hayashi, Correlation between the spin Hall angle and the structural phases of early 5 d transition metals, Appl Phys Lett **107**, 232408 (2015).

[11] Y. Takeuchi, C. Zhang, A. Okada, H. Sato, S. Fukami, and H. Ohno, Spin-orbit torques in high-resistivity-W/CoFeB/MgO, Appl Phys Lett **112**, 192408 (2018).

[12] Q. Hao and G. Xiao, Giant Spin Hall Effect and Switching Induced by Spin-Transfer Torque in a W/Co40Fe40 B20/MgO Structure with Perpendicular Magnetic Anisotropy, Phys Rev Appl **3**, 034009 (2015).

[13] C. F. Pai, L. Liu, Y. Li, H. W. Tseng, D. C. Ralph, and R. A. Buhrman, Spin transfer torque devices utilizing the giant spin Hall effect of tungsten, Appl Phys Lett **101**, 122404 (2012).

[14] A. Ghosh, H. J. Chung, K. H. Khoo, J. Shanmugam, J. Qiu, S. Allauddin, and S. Ter Lim, Probing the Spin Hall Characteristics of W/CoFeB/MgO Based Heterostructures for Spin-Orbit Torque Based Magnetic Random Access Memory Application, Adv Electron Mater **8**, 2100982 (2022).

[15] W. Chen, G. Xiao, Q. Zhang, and X. Zhang, Temperature study of the giant spin Hall effect in the bulk limit of β- W, Phys Rev B **98**, 134411 (2018).

[16] K. K. Vudya Sethu, S. Ghosh, S. Couet, J. Swerts, B. Sorée, J. De Boeck, G. S. Kar, and K. Garello, Optimization of Tungsten β -Phase Window for Spin-Orbit-Torque Magnetic Random-Access Memory, Phys Rev Appl **16**, 064009 (2021).

[17] K. U. Demasius, T. Phung, W. Zhang, B. P. Hughes, S. H. Yang, A. Kellock, W. Han, A. Pushp, and S. S. P. Parkin, Enhanced spin-orbit torques by oxygen incorporation in tungsten films, Nat Commun **7**, 10644 (2016).

[18] O. L. W. McHugh, W. F. Goh, M. Gradhand, and D. A. Stewart, Impact of impurities on the spin Hall conductivity in β -W, Phys Rev Mater **4**, 094404 (2020).

[19] A. Chattaraj, M. Balal, A. K. Yadav, S. R. Barman, A. K. Sinha, S. N. Jha, S. Joulie, V. Serin, A. Claverie, V. Kumar et al., Unravelling oxygen driven α to β phase transformation in tungsten, Sci Rep **10**, 14718 (2020).

[20] Q. Shao, P. Li, L. Liu, H. Yang, S. Fukami, A. Razavi, H. Wu, K. Wang, F. Freimuth, Y. Mokrousov et al., Roadmap of Spin-Orbit Torques, IEEE Trans Magn **57**, 1 (2021).

[21] G. Kresse and J. Furthmiiller, Efficiency of ab-initio total energy calculations for metals and semiconductors, Comput Mater Sci **6**, 15 (1996).

[22] J. Qiao, J. Zhou, Z. Yuan, and W. Zhao, Calculation of intrinsic spin Hall conductivity by Wannier interpolation, Phys Rev B **98**, 214402 (2018).

[23] A. A. Mostofi, J. R. Yates, G. Pizzi, Y.-S. Lee, I. Souza, D. Vanderbilt, and N. Marzari, An updated version of wannier90: A tool for obtaining maximally-localised Wannier functions, Comput. Phys. Commun. **185**, 2309 (2014).

[24] J. Lourembam, X. Yu, M. P. R. Sabino, R. Sabino, M. Tran, R. W. T. Ang, Q. J. Yap, S. Ter Lim, and A. Rusydi, Critical Role of Capping Layer in Determining Co-Fe-B / MgO Interfacial Magnetism Revealed by X-Ray Magnetic Circular Dichroism, Phys Rev Appl **14**, 054022 (2020).

[25] J. F. Van Der Veen, ION BEAM CRYSTALLOGRAPHY OF SURFACES AND INTERFACES, Surf Sci Rep **5**, 199 (1985).

[26] C. Jeynes, N. P. Barradas, P. K. Marriott, G. Boudreault, M. Jenkin, E. Wendler, and R. P. Webb, Elemental thin film depth profiles by ion beam analysis using simulated annealing-a new tool, J. Phys. D: Appl. Phys **36**, 97 (2003).

[27] H. Yan, H. Mao, P. Qin, J. Wang, H. Liang, X. Zhou, X. Wang, H. Chen, Z. Meng, L. Liu et al., An antiferromagnetic spin phase change memory, Nat Commun **15**, 4978 (2024).

[28] M. Hayashi, J. Kim, M. Yamanouchi, and H. Ohno, Quantitative characterization of the spin-orbit torque using harmonic Hall voltage measurements, Phys Rev B Condens Matter Mater Phys **89**, (2014).

[29] K. Garello, I. M. Miron, C. O. Avci, F. Freimuth, Y. Mokrousov, S. Blügel, S. Auffret, O. Boulle, G. Gaudin, and P. Gambardella, Symmetry and magnitude of spin-orbit torques in ferromagnetic heterostructures, Nat Nanotechnol **8**, 587 (2013).

[30] L. Huang, S. He, Q. J. Yap, and S. Ter Lim, Engineering magnetic heterostructures to obtain large spin Hall efficiency for spin-orbit torque devices, Appl Phys Lett **113**, 022402 (2018).

[31] J. Lourembam, L. Huang, B. Chen, J. Qiu, H. J. Chung, S. L. K. Yap, Q. J. Yap, S. K. Wong, and S. Ter Lim, Multi-State Magnetic Tunnel Junction Programmable by Nanosecond Spin-Orbit Torque Pulse Sequence, Adv Electron Mater **7**, 2001133 (2021).

[32] R. H. Koch, J. A. Katine, and J. Z. Sun, Time-Resolved Reversal of Spin-Transfer Switching in a Nanomagnet, Phys Rev Lett **92**, 088302 (2004).

[33] D. Apalkov, B. Dieny, and J. Slaughter, *Magnetoresistive Random Access Memory*, in *Proc. IEEE*, Vol. 104 (2016), pp. 1796–1830.

[34] L. Liu, C.-F. Pai, Y. Li, H. W. Tseng, D. C. Ralph, and R. A. Buhrman, Spin-Torque Switching with the Giant Spin Hall Effect of Tantalum, Science (1979) **336**, 555 (2012).

[35] P. E. Blochl, Projector augmented-wave method, Phys Rev B **50**, 17953 (1994).

[36] J. P. Perdew, K. Burke, and M. Ernzerhof, Generalized Gradient Approximation Made Simple - The PBE functional, Phys Rev Lett **77**, 3865 (1996).

[37] Hendrik J. Monkhorst, Special points for Brillouin-zone integretions, Phys Rev B **13**, 5188 (1976).

[38] S. Fukami, T. Anekawa, C. Zhang, and H. Ohno, A spin-orbit torque switching scheme with collinear magnetic easy axis and current configuration, Nat Nanotechnol **11**, 621 (2016).